Decadal Modulation of the ENSO–Indian Ocean Basin Warming Relationship during the Decaying Summer by the Interdecadal Pacific Oscillation

FANGYU LIU,[a] WENJUN ZHANG,[a] FEI-FEI JIN,[b] AND SUQIONG HU[a]

[a] *Collaborative Innovation Center on Forecast and Evaluation of Meteorological Disasters, Key Laboratory of Meteorological Disaster of Ministry of Education, Nanjing University of Information Science and Technology, Nanjing, China*
[b] *Department of Meteorology, School of Ocean and Earth Science and Technology, University of Hawai'i at Mānoa, Honolulu, Hawaii*

(Manuscript received 15 June 2020, in final form 30 November 2020)

ABSTRACT: Many previous studies have shown that an Indian Ocean basin warming (IOBW) occurs usually during El Niño–Southern Oscillation (ENSO) decaying spring to summer seasons through modifying the equatorial zonal circulation. Decadal modulation associated with the interdecadal Pacific oscillation (IPO) is further investigated here to understand the nonstationary ENSO–IOBW relationship during ENSO decaying summer (July–September). During the positive IPO phase, significant warm sea surface temperature (SST) anomalies are observed over the tropical Indian Ocean in El Niño decaying summers and vice versa for La Niña events, while these patterns are not well detected in the negative IPO phase. Different decaying speeds of ENSO associated with the IPO phase, largely controlled by both zonal advective and thermocline feedbacks, are suggested to be mainly responsible for these different ENSO–IOBW relationships. In contrast to ENSO events in the negative IPO phase, the ones in the positive IPO phase display a slower decaying speed and delay their transitions both from a warm to a cold state and a cold to a warm state. The slower decay of El Niño and La Niña thereby helps to sustain the teleconnection forcing over the equatorial Indian Ocean and corresponding SST anomalies there can persist into summer. This IPO modulation of the ENSO–IOBW relationship carries important implications for the seasonal prediction of the Indian Ocean SST anomalies and associated summer climate anomalies.

KEYWORDS: Indian Ocean; Atmosphere-ocean interaction; ENSO; Pacific decadal oscillation

1. Introduction

The predominant mode of global interannual climate variability is El Niño–Southern Oscillation (ENSO), which arises from large-scale coupled ocean–atmosphere interactions in the tropical Pacific (e.g., Bjerknes 1969; Wyrtki 1975; Cane and Zebiak 1985; Jin 1997; Neelin et al. 1998). ENSO has widespread climate impacts around the globe via atmospheric teleconnections (e.g., Wang et al. 2000; Alexander et al. 2002; Lau and Nath 2003), providing a potential forecasting skill for regional climate anomalies in seasonal-to-interannual time scales. For instance, ENSO affects the climate over North America via the Pacific–North American (PNA) teleconnection pattern (Wallace and Gutzler 1981; Trenberth et al. 1998). ENSO exerts strong impacts on the East Asian climate through modulating the atmospheric circulation over the western North Pacific (WNP) (e.g., Harrison and Larkin 1996; Zhang et al. 1996; Wang et al. 2000; Watanabe and Jin 2002; Yang et al. 2007; Xie et al. 2009; Stuecker et al. 2015; Zhang et al. 2016).

ENSO-induced sea surface temperature anomalies (SSTAs) can also be observed in tropical oceans owing to the anomalous Walker circulation (e.g., Klein et al. 1999; Alexander et al. 2002; Wang 2019). During El Niño autumns, strong dipole SSTAs sometimes appear in the tropical Indian Ocean (IO) (Saji et al. 1999; Webster et al. 1999). When El Niño enters its peak during winter, the Indian Ocean dipole structure disappears and is changed to Indian Ocean basin warming (IOBW), referred to as the Indian Ocean basin mode (Li et al. 2003; Yang et al. 2007; Xie et al. 2009). This basin warming reaches its peak usually in spring and decays in subsequent seasons (e.g., Nigam and Shen 1993; Klein et al. 1999; Lau and Nath 2003). Surface heat fluxes, specifically the latent heat flux and shortwave radiation, are largely responsible for the warming in much of the equatorial IO (Klein et al. 1999; Alexander et al. 2002), except for the southwestern IO (SWIO) with ocean dynamics involved (Xie et al. 2002; Schott et al. 2009). The El Niño–related anticyclonic anomalies over the southeastern IO can force downwelling Rossby waves, which propagate westward and deepen the thermocline in the SWIO, contributing considerably to the SWIO warming (Xie et al. 2002; Du et al. 2009). This warming can further enhance the local tropical IO warming, especially over the northern part, through exciting equatorially antisymmetric wind anomalies (e.g., Wu et al. 2008; Wu and Yeh 2010; Chakravorty et al. 2012). These observed ENSO teleconnections to the tropical IO can be reproduced in most coupled models (Saji et al. 2006; Du et al. 2013).

Recent studies documented that the ENSO–IOBW relationship exhibits a decadal variation (e.g., Huang et al. 2010; Xie et al. 2010; Chowdary et al. 2012, 2014; Tao et al. 2015). The El Niño–associated IOBW can be significantly observed during the summer season after the 1970s. However, this robust IO warming cannot persist through the El Niño decaying summer before the 1970s (e.g., Huang et al. 2010; Xie et al. 2010;

Corresponding author: Wenjun Zhang, zhangwj@nuist.edu.cn

DOI: 10.1175/JCLI-D-20-0457.1

Chowdary et al. 2012). This decadal variation can be captured in historical simulations of some coupled models (Du et al. 2013; Tao et al. 2015). The changed ENSO–IOBW relationship is argued to be possibly related to the ENSO variance (e.g., Xie et al. 2010, 2016; Chowdary et al. 2012; Yang et al. 2015). ENSO variance is increased after the 1970s, favoring a relatively stronger ENSO teleconnection to the IO. Concurrently, a shallower SWIO dome partially contributes to the stronger ENSO–IOBW relationship after the 1970s by enhancing the local thermocline feedback (e.g., Xie et al. 2010; Chowdary et al. 2012; Tao et al. 2015).

The decadal change of the interannual relationships is usually modulated by low-frequency multidecadal variabilities, such as the Atlantic multidecadal oscillation (AMO) (Knight 2005) and interdecadal Pacific oscillation (IPO) (Mantua et al. 1997; Power et al. 1999). The AMO, as a natural mode in the North Atlantic Ocean with a period of about 60–80 years, exerts substantial impacts on the relationship between ENSO and the Indo-western Pacific climate (e.g., Lu et al. 2008; Chen et al. 2010; Geng et al. 2017, 2018). The IPO, the leading mode of SST variability over the Pacific at a multidecadal time scale, has also been proposed to play an important role in ENSO teleconnections to other climate signals over many regions, such as East Asia (e.g., Wang et al. 2008; Feng et al. 2014; Watanabe and Yamazaki 2014). Whether these multidecadal natural modes modulate the ENSO–IOBW relationship remains open to be answered. If their relationship is determined by these multidecadal modes, it will provide a useful prediction skill for the tropical IO climate. The 1970s' shift of the ENSO–IOBW relationship, concurrent with an IPO phase transition, holds a clue that the IPO could modulate their relationship.

In the present study, the long-term reanalysis data for the period of 1900–2018 are utilized to investigate possible multidecadal modulations of the natural modes on the ENSO–IOBW relationship. Our results show that the IPO variability is mainly responsible for the changed relationship of the ENSO–IOBW during the ENSO decaying summer. In the remainder of the paper, section 2 introduces the datasets and methods. Section 3 reports the nonstationary feature of the ENSO–IOBW relationship and its modulation by the IPO. Furthermore, possible mechanisms are discussed in section 4. The major conclusions and discussion are summarized in section 5.

2. Data and methodology

Monthly SSTA associated with ENSO is examined based on the Hadley Centre sea ice and SST dataset (HadISST) version 1.1 during 1900–2018 (Rayner et al. 2003). The atmospheric circulation is investigated using the National Oceanic and Atmospheric Administration–Cooperative Institute for Research in Environmental Sciences (NOAA-CIRES) Twentieth Century Reanalysis V2c dataset for the period of 1900–2014 (Compo et al. 2011). The heat flux is derived from the ERA5 (the fifth generation of ECMWF atmospheric reanalyses of the global climate) for the period of 1979–2018 (Hersbach et al. 2020). The ocean currents and subsurface temperature are taken from the Simple Ocean Data Assimilation ocean sea/ice reanalysis (SODA) version 3.3.1 for the period of 1980–2015 (Carton et al. 2018). Preindustrial control (pi-Control) simulations of 20 climate models are obtained from phase 5 of the Coupled Model Intercomparison Project (CMIP5) (Table 2). Monthly output of SST is utilized here, and the last 100 years of each model are chosen for analyses.

Several normalized climatic indices are utilized to facilitate our analyses. The Niño-3.4 index is defined as the area-averaged SSTA in the region of 5°S–5°N and 120°–170°W for the boreal winter season [December–February (DJF)]. The annual mean IPO index is measured as the difference between the SSTA in the central equatorial Pacific (10°S–10°N, 170°E–90°W) and those in the northwest (25°–45°N, 140°E–145°W) and southwest Pacific (50°–15°S, 150°E–160°W), following the previous study (Henley et al. 2015). The annual mean AMO index, defined as the area-averaged SSTA over the North Atlantic (Enfield et al. 2001), is provided by NOAA (https://www.esrl.noaa.gov/psd/data/correlation/amon.us.long.data).

Our analyses focus on the period of 1900–2018 and anomalies for all variables are computed as the deviations from the climatological mean over the entire period. To highlight the ENSO-related interannual variability, a 6–120-month bandpass Lanczos filter (Duchon 1979) is applied on each dataset. A threshold of ± 0.6 standard deviations of the DJF Niño-3.4 index is used to define ENSO events. Here, ENSO events are labeled year(0)/year(1), where 0 and 1 denote the ENSO developing and decaying year, respectively. For consecutive La Niña events, only the last year is selected for analyses since the ENSO decay phase is investigated here. Statistical significance is determined using the two-tailed Student's t test. Considering possible impacts of super El Niño events (e.g., 1997/98 event), we re-examine our results by excluding these super events and qualitative conclusions remain the same.

3. Decadal modulation of the ENSO–IOBW relationship by the IPO

To examine possible modulation of the ENSO–IOBW relationship by the IPO, Fig. 1 shows the regressed SST and 850-hPa wind anomalies upon the DJF Niño-3.4 index in different IPO phases. For both positive and negative IPO phases, ENSO exhibits similar teleconnections to the IO with a dipole SSTA structure and basin warming during its developing autumns and mature winters, respectively (Figs. 1a,b,e,f). During decaying spring, the ENSO signal can be well detected in the IO SSTA for both IPO phases despite some differences in the amplitude (Figs. 1c,g). The corresponding regressed wind anomalies during the positive IPO phase exhibit an equatorially antisymmetric pattern dominated by easterly and westerly anomalies north and south of the equator, respectively (Fig. 1c), consistent with previous studies (Du et al. 2009). In contrast, this antisymmetric wind anomaly pattern cannot be clearly seen during the negative IPO phase (Fig. 1g). These different wind anomalies seem to have important impacts on IO SSTA during the next seasons considering relatively long ocean memory. In comparison with preceding seasons, the

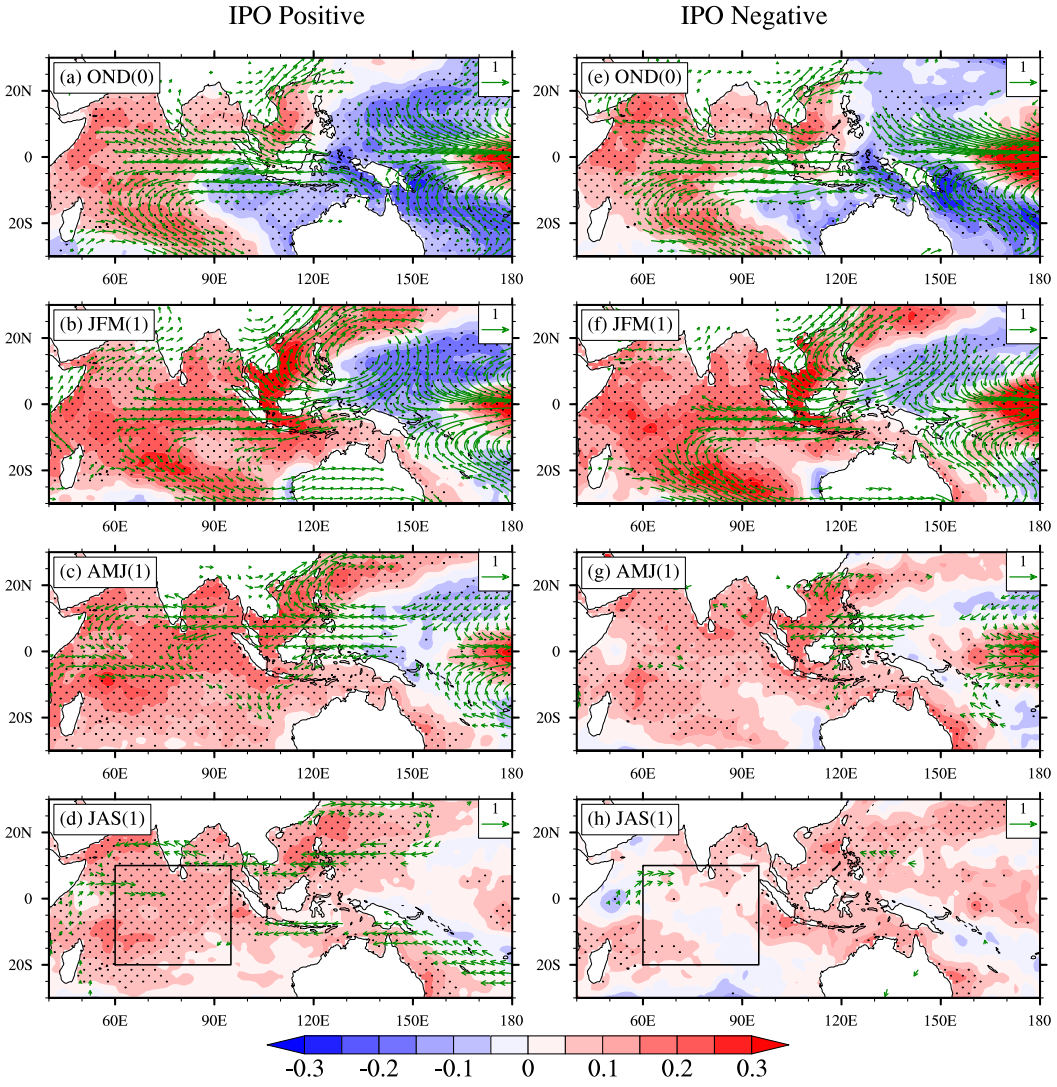

FIG. 1. Regressed SST (shading; °C) and 850-hPa horizontal wind (vectors; m s^{-1}) anomalies with respect to the normalized D(0)JF(1) Niño-3.4 index for the positive IPO phase (1900–45 and 1981–97) in (a) October–December [OND(0)], (b) January–March [JFM(1)], (c) April–June [AMJ(1)], and (d) July–September [JAS(1)]. (e)–(h) As in (a)–(d), but for the negative IPO phase (1946–80 and 1998–2014). The region marked with the black box in (d) and (h) is used to describe the tropical Indian Ocean SSTA index (TIOI). Stippling represents SST values above the 95% confidence level. The wind anomalies are displayed only when they are significant at the 95% confidence level.

ENSO events are accompanied with very different IO SSTA responses in its decaying summer [July–September (JAS)] (Figs. 1d,h). The ENSO-associated IOBW persists into summer in the positive IPO phase, concurrent with significant WNP anticyclonic anomalies (Fig. 1d), which is usually argued to be associated with the IO capacitor mechanism despite of ongoing debate (e.g., Wang et al. 2000; Xie et al. 2009; Stuecker et al. 2015; Chen et al. 2016; Zhang et al. 2016). However, this IOBW is observed only during winter and spring in the negative IPO phase and disappears in summer (Fig. 1h). Regression maps for the individual months of summer are further examined, and each of them is similar to the JAS mean despite of small differences (not shown). In next analyses, we focus on the summer (JAS) of the ENSO decaying phase considering distinctive IO SST responses.

For convenience, we define the SSTA in the tropical IO (TIO; 20°S–10°N, 60°–95°E; black box in Figs. 1d and 1h) as an index (TIOI) to further investigate the IOBW's relation with the ENSO. The qualitative conclusions remain the same when the adjacent regions are considered. Figure 2 displays the DJF Niño-3.4 index and the subsequent JAS TIOI from 1901–2018 to confirm the IPO modulation of the ENSO–IOBW relationship. These two indices exhibit pronounced interannual variability with a positive correlation (R = 0.44, significant at the 95% confidence). It suggests that El Niño events are usually accompanied by warm SSTA over the IO during its

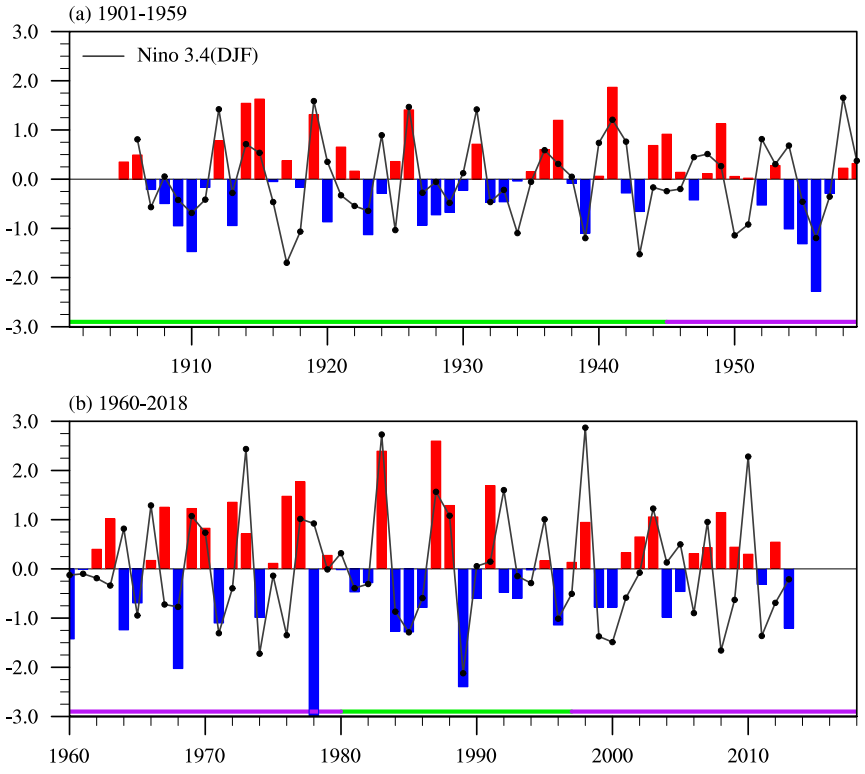

FIG. 2. Time series of the normalized D(0)JF(1) Niño-3.4 index (dotted curve) and JAS(1) TIOI (bar) during (a) 1901–59 and (b) 1960–2018. The green and purple lines represent the positive and negative IPO phases, respectively.

decaying summer and vice versa for La Niña events, consistent with previous studies (e.g., Weare 1979; Alexander et al. 2002; Liu and Alexander 2007; Xie et al. 2009). However, this positive correlation displays highly unstable features. During the positive IPO phase marked with green lines, most El Niño and La Niña events coincide with warm and cold IO SSTA, respectively (Fig. 2). It is not the case for the negative IPO phase marked with purple lines. Different from our common recognitions, even cold and warm SSTAs appear in the IO during some El Niño (e.g., 1963/64 and 1977/78) and La Niña (e.g., 1975/76 and 2008/09) events, respectively.

A 17-yr running correlation is used to detect the nonstationary relationship between ENSO and IOBW (Fig. 3, colored solid curve). Here, the results are not sensitive to the sliding window selected, such as 15- and 19-yr variations. The 9-yr running averaged IPO (bar) and AMO (gray dashed curve)

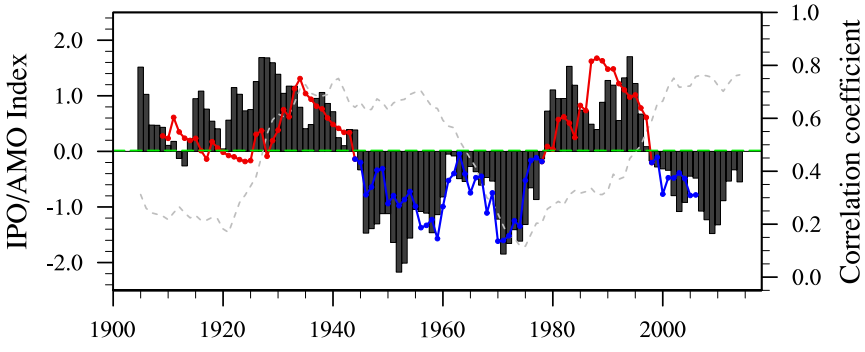

FIG. 3. The 9-yr running averaged IPO index (bar) and AMO index (gray dashed curve), and 17-yr sliding correlation between the D(0)JF(1) Niño-3.4 index and JAS(1) TIOI (colored solid curve) during 1900–2018. The horizontal green dashed line indicates the 95% significance level for the correlation. The red and blue color solid curves represent the correlation above and below the 95% confidence level, respectively.

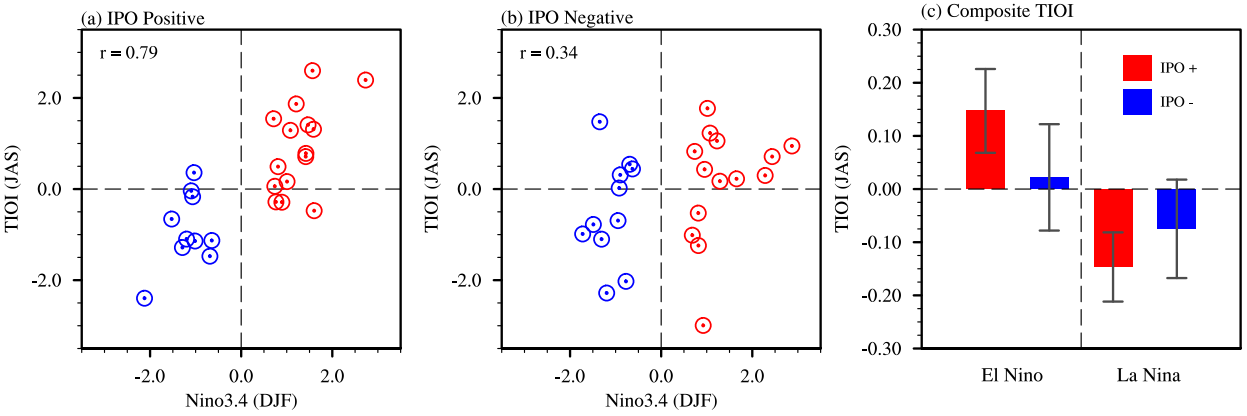

FIG. 4. (a) Scatterplot of the JAS(1) TIOI as a function of the normalized D(0)JF(1) Niño-3.4 index for the El Niño (red circle) and La Niña (blue circle) events during the positive IPO phase. (b) As in (a), but during the negative IPO phase. (c) Composite JAS(1) TIOI (°C) of the El Niño and La Niña events during different IPO phases. The error bars represent one standard deviation.

indices are also shown in Fig. 3 to investigate their potential modulation of the ENSO–IOBW relationship. It is shown that ENSO and IOBW are statistically significantly correlated before the early 1940s and in the 1980s–90s based on the 95% confidence level, while nonsignificant correlation is observed during other periods. The AMO switches from negative to positive in the middle 1920s and 1990s, and from positive to negative in the middle 1960s (Fig. 3). The AMO does not vary consistently with the running correlation between ENSO and IOBW [R(AMO, the running correlation) = 0.17]. In contrast, the IPO exhibits consistently temporal evolutions with the variations of the ENSO–IOBW relationship [R(IPO, the running correlation) = 0.78], suggesting that the ENSO–IOBW relationship is likely modulated by the IPO. During the positive IPO phase, ENSO has a strong impact on the IO SST in its decaying summer, while a very weak IO SST response is shown during the negative IPO phase.

We also show the scatterplot of the DJF Niño-3.4 and JAS TIOI in the positive and negative IPO phases, respectively (Figs. 4a,b). Most El Niño and La Niña events in the positive IPO phase are accompanied by warm and cold IO basin SSTA, respectively. Their linear correlation coefficient is 0.79, exceeding the 95% confidence level. However, no simple relationship is detected during the negative IPO phase. About 30% of El Niño decaying summers experienced negative SSTA in the IO, and nearly half of La Niña events correspond to positive IO SSTA, both of which contribute to the weak ENSO–IOBW correlation during the negative IPO phase. Furthermore, the asymmetric features are also displayed in the composite results (Fig. 4c). During the positive IPO phase, both El Niño and La Niña events are robustly associated with the IO SSTA. On the other hand, both El Niño and La Niña composite IO SSTA display small values with relatively large standard deviation during the negative IPO phase, suggesting that the ENSO–IOBW relationship is complicated.

4. Possible modulation mechanisms by the IPO

a. *Changes of ENSO evolution and associated large-scale atmospheric circulation*

Section 3 has shown that the ENSO–IOBW relationship is highly related to the IPO phase. It is easy to hypothesize that their nonstationary relationship could be due to different ENSO features in different IPO phases. To examine possible impacts of the IPO on the ENSO feature, we categorize ENSO events into four types: El Niño during a positive IPO phase (IPO+/El Niño) and a negative phase (IPO−/El Niño), and La Niña during a positive IPO phase (IPO+/La Niña) and a negative phase (IPO−/La Niña) (Table 1). Figure 5 displays the composite evolutions of the SST and wind anomalies for

TABLE 1. El Niño and La Niña years classified based on IPO phases for the period 1900–2018. Note only the last year is selected for consecutive La Niña events.

	El Niño years	La Niña years
Positive IPO	1905/06, 1911/12, 1913/14, 1918/19, 1923/24, 1925/26, 1930/31, 1939/40, 1940/41, 1941/42, 1982/83, 1986/87, 1987/88, 1991/92, 1994/95	1909/10, 1917/18, 1922/23, 1924/25, 1933/34, 1938/39, 1942/43, 1984/85, 1988/89, 1995/96
Negative IPO	1951/52, 1953/54, 1957/58, 1963/64, 1965/66, 1968/69, 1969/70, 1972/73, 1976/77, 1977/78, 1997/98, 2002/03, 2006/07, 2009/10	1950/51, 1955/56, 1964/65, 1967/68, 1970/71, 1973/74, 1975/76, 1999/00, 2005/06, 2008/09, 2011/12

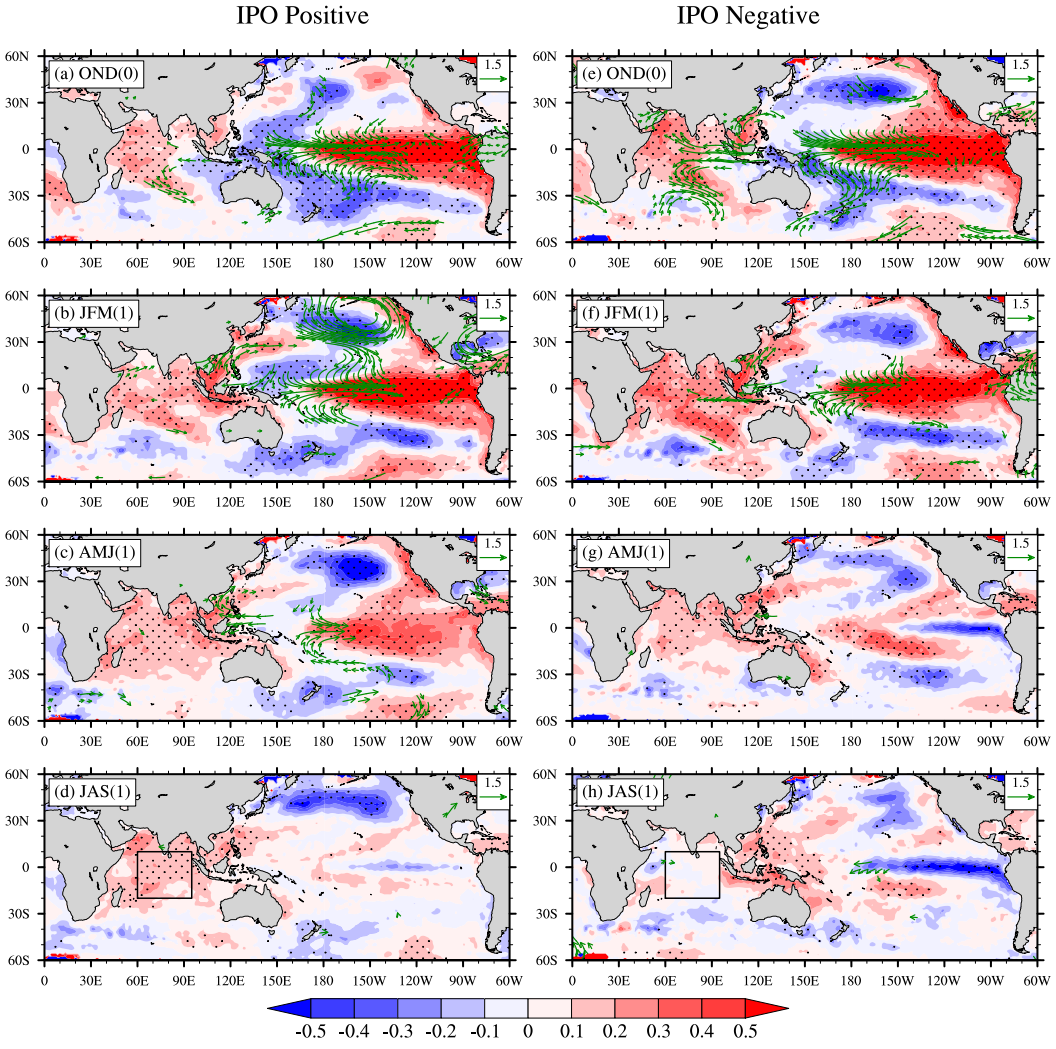

FIG. 5. Composite SST (shading; °C) and 850-hPa horizontal wind (vectors; m s^{-1}) anomalies for the El Niño peaking and decaying seasons in (a) OND(0), (b) JFM(1), (c) AMJ(1), and (d) JAS(1) during the positive IPO phase. (e)–(h) As in (a)–(d), but during the negative IPO phase. Stippling represents SSTA values above the 95% confidence level. The wind anomalies are displayed only when they are significant at the 95% confidence level.

the IPO+/El Niño and IPO−/El Niño events from the winter to following summer. For the IPO+/El Niño composite, strongly warm SSTA occurs in the tropical central and eastern Pacific during winter, then decays during the following seasons, and eventually disappears in the summer (Fig. 5d). Concurrently, the Indian Ocean dipole SSTA structure forms in the autumn during the ENSO developing phase (Fig. 5a), through the ENSO-related atmospheric forcing and local Bjerknes feedback (e.g., Annamalai et al. 2003; Krishnamurthy and Kirtman 2003; Yu and Lau 2004). In the following winter and spring when the equatorial climatological winds reverse their directions with monsoon transitions (Li et al. 2003), the IO builds up to a basin warming and these warm SST maintain their anomalies till the end of summer (Figs. 5b–d). The warm SST persistence could be associated with the ocean memory and ENSO-related atmospheric forcing.

For the IPO−/El Niño composite, the positive SSTA decays rapidly and negative SSTA appears in the equatorial eastern Pacific during spring (Fig. 5g), approximately two months earlier than that of the IPO+/El Niño composite. This negative SSTA is strengthened in summer, which could exert very different influence on the IO compared to the warming SSTA in Fig. 5c via the zonal circulation. Figure 6 shows the anomalous Walker circulation for El Niño decaying years during the positive and negative IPO phases. For the IPO+/El Niño composite, anomalous ascending motions are observed in the central Pacific during spring (Fig. 6a) and are replaced by weak descending motions in the following summer (Fig. 6c) since El Niño–induced SSTA returns to a relatively weak negative state

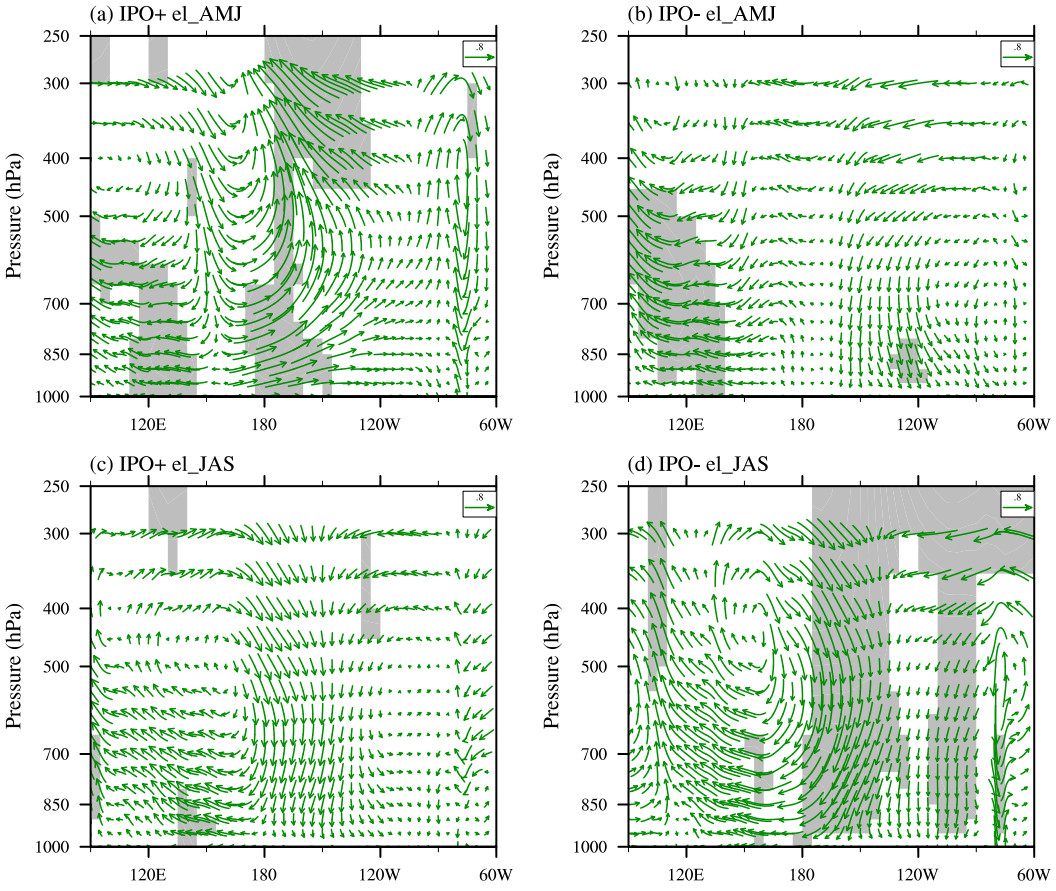

FIG. 6. Composite equatorial (5°S–5°N) Walker circulation anomalies [vectors; m s^{-1}; the anomalous vertical velocity (Pa s^{-1}) is multiplied by a factor of −100] for the El Niño decaying years in (a) AMJ(1) and (c) JAS(1) during the positive IPO phase. (b),(d) As in (a) and (c), but during the negative IPO phase. Shading is shown when the zonal or vertical wind anomalies are significant at the 95% confidence level.

(Fig. 5d). In contrast, accompanied by a rapid decaying SSTA in the central and eastern Pacific for the IPO−/El Niño, weak descending motions have emerged during spring (Fig. 6b) and are further amplified in the following summer (Fig. 6d). The negative SSTA in the eastern Pacific thus exerts strong impacts on the IO via a strengthened Walker circulation and the associated negative heat flux anomalies are not conducive to the maintenance of warming in the IO, which is shown in Fig. 7. In contrast, positive heat flux anomalies are observed in the IO during El Niño decaying spring in the positive IPO phase, which promotes the maintenance of IOBW toward summer (Fig. 7). In a parallel way, composite analyses for La Niña events with different IPO phases are also carried out and similar conclusions are derived (Figs. 7 and 8). During the negative IPO phase, the fast decay is evident and SSTA is changed to warm anomalies in the eastern Pacific during the decaying spring and summer seasons (Fig. 8g). In comparison, the preceding cold SSTAs for La Niña events in the positive IPO phase can persist longer to summer (Fig. 8d) and the slow decay helps to sustain the teleconnection forcing longer over the equatorial IO (Fig. 7).

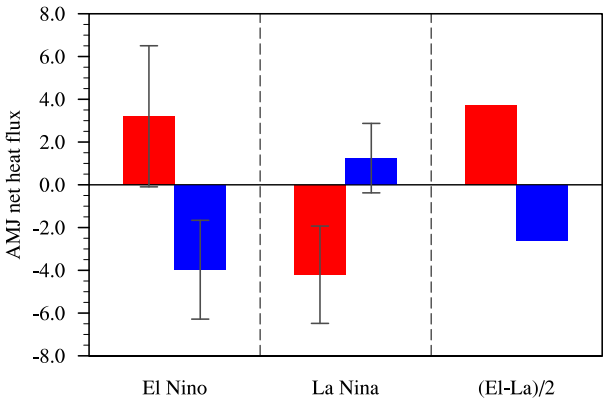

FIG. 7. Composite AMJ(1) net heat flux anomalies (W m^{-2}) over the region (20°S–10°N, 60°–95°E) for El Niño events and La Niña events, and their difference (shown from left to right) during the positive (red bar) and negative (blue bar) IPO phases. The error bars represent one standard deviation.

Figures 9a and 9b shows the seasonal evolutions of the Niño-3.4 index to clearly describe different ENSO evolutions for the positive and negative IPO phases. The IPO+/El Niño initiates in early summer, peaks in January, and decays in the following boreal spring. In the decaying summer, the SSTA is near zero with high uncertainty (Fig. 9a). In contrast to the IPO+/El

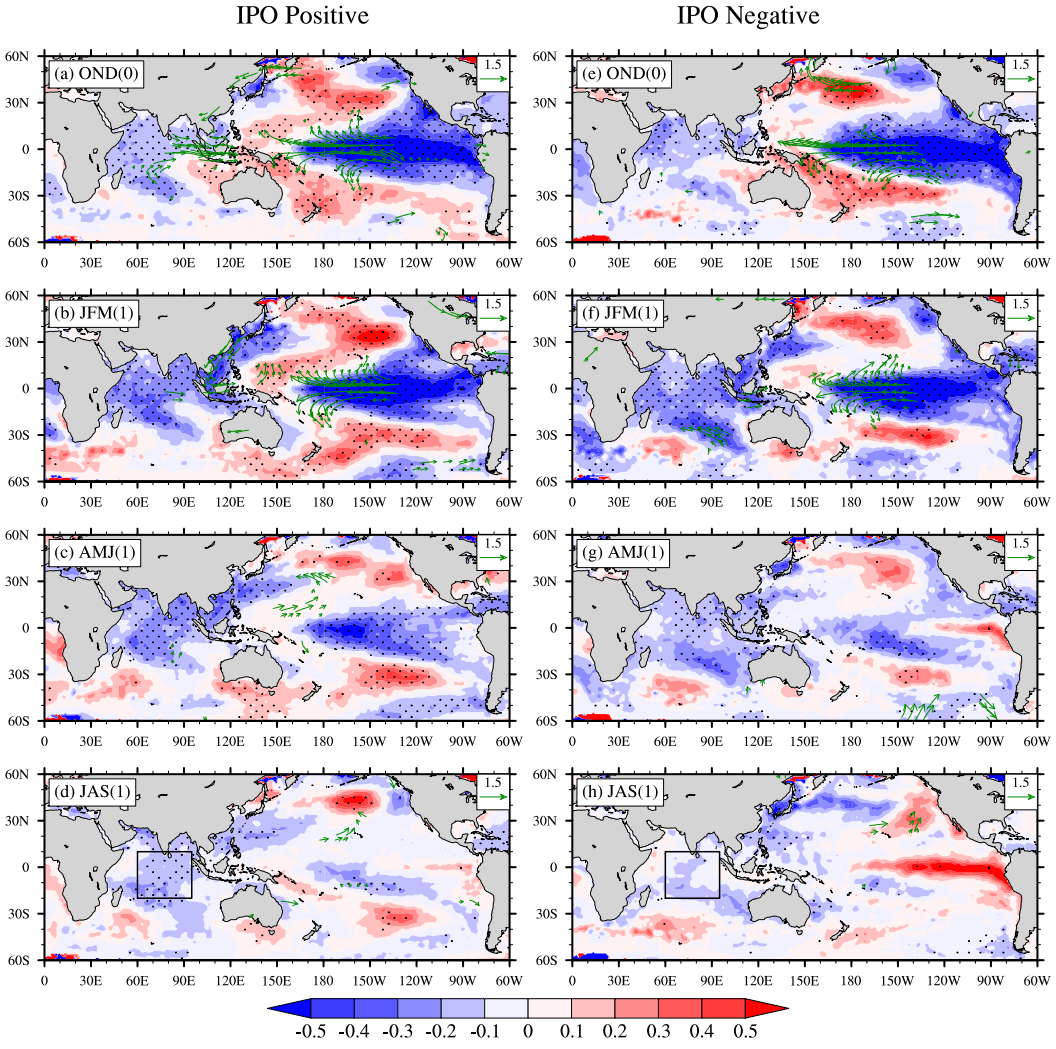

FIG. 8. As in Fig. 5, but for the La Niña years.

Niño, the IPO−/El Niño reaches its maximum with one-month lead and decays more rapidly. Correspondingly, the IPO−/El Niño events return to a normal state about two months in advance and switch into a La Niña condition in the post–El Niño summer. We also calculate the decaying speed from the peaking month to the normal state when the Niño-3.4 index is close to zero, and a higher decaying speed is observed in the negative IPO phase (-0.21°C month^{-1}) than that in the positive phase (-0.15°C month^{-1}). A similar phenomenon is evident in the La Niña composite. The IPO−/La Niña events reach a normal state two months in advance compared with the IPO+/La Niña (Fig. 9b). An El Niño–like SSTA pattern develops during the decaying summer of the IPO−/La Niña, while a normal state is observed in the tropical Pacific during the decaying summer of the IPO+/La Niña. We also display in Figs. 9c and 9d the ENSO-associated TIOI evolutions in different IPO phases. The IOBW exhibits a roughly similar evolution with the ENSO but with about a 2–3-month lag, consistent with the lagged IO SST response to the ENSO-associated atmospheric forcing. Different decaying features are observed for the IOBW, corresponding to the El Niño evolutions. For the IPO+/El Niño with slow decaying speed, the IOBW persists into late summer (Fig. 9c), while a normal IO state is shown for the IPO−/El Niño. The same case is displayed for La Niña with different IPO phases (Fig. 9d). These results suggest that the decaying speed of ENSO associated with the IPO phase has an important role on the IO SSTA, especially in ENSO decaying summer, and thus regulates the ENSO–IOBW relationship.

b. Dynamical processes controlling the ENSO decaying speed

To understand possible effects of different IPO phases on the ENSO decaying speed, we conduct heat budget analyses on the mixed layer sea temperature in the upper 45 m of the tropical Pacific based on the SODA data. The anomalous

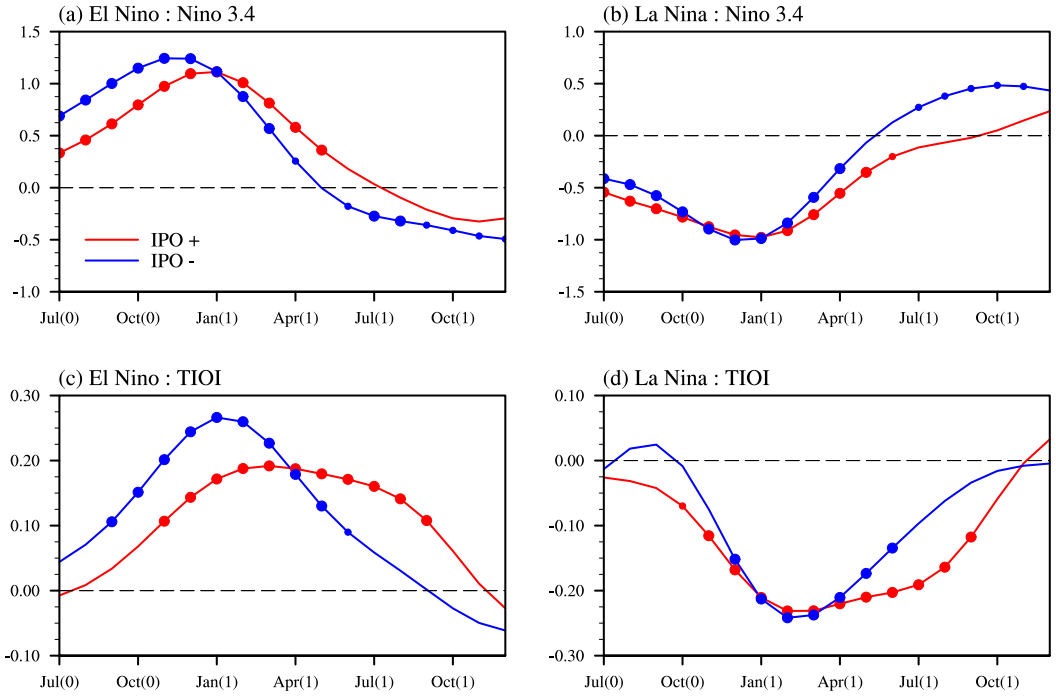

FIG. 9. Composite evolution of the Niño-3.4 indices during the positive (red curve; °C) and negative (blue curve; °C) IPO phases for (a) El Niño and (b) La Niña events. (c),(d) As in (a) and (b), but for composite evolution of the TIOI. Small and big dots represent the values exceeding the 90% and 95% confidence levels, respectively.

budget equation follows our previous studies (e.g., An and Jin 2004; Zhang et al. 2013):

$$\frac{\partial T_a}{\partial t} = -U_c\frac{\partial T_a}{\partial x} - U_a\frac{\partial T_c}{\partial x} - U_a\frac{\partial T_a}{\partial x} - V_c\frac{\partial T_a}{\partial y} - V_a\frac{\partial T_c}{\partial y} - V_a\frac{\partial T_a}{\partial y} - W_c\frac{\partial T_a}{\partial z} - W_a\frac{\partial T_c}{\partial z} - W_a\frac{\partial T_a}{\partial z} + \frac{Q_a}{\rho_0 C_p H} + R \quad (1)$$

Here, the subscripts c and a indicate the climatological mean and corresponding anomalies, respectively; T, U, and V represent the oceanic temperature and the zonal and meridional current velocities, respectively. The vertical current velocity W is calculated at the bottom of the mixed layer H, which is defined as 45 m in our calculation. The qualitative conclusions remain unchanged even if we use other depths, such as 60 m. The term Q_a denotes the anomalous net surface heat flux expressed as the sum of the shortwave, longwave, latent, and sensible heat flux. The residual term R includes contributions from diffusion, subgrid-scale time processes, and potential errors in each term computation.

Our study focuses on the decay phase of ENSO spanning the five months from February to June, which is the key stage of the ENSO decay. Figure 10 shows each budget term of El Niño minus La Niña composites over the equatorial Pacific (3°S–3°N, 160°E–110°W) in different IPO phases. The Niño-3.4 region is also examined and qualitative results remain the same. Different physical processes contribute to the sea temperature tendency differently, among which the two most important terms are the zonal advection of mean temperature by anomalous current $[U_a(\partial T_c/\partial x)]$ and the vertical advection of anomalous subsurface temperature by mean upwelling $[W_c(\partial T_a/\partial z)]$. These two terms, referred to as zonal advective and thermocline feedbacks, are in phase with the temperature

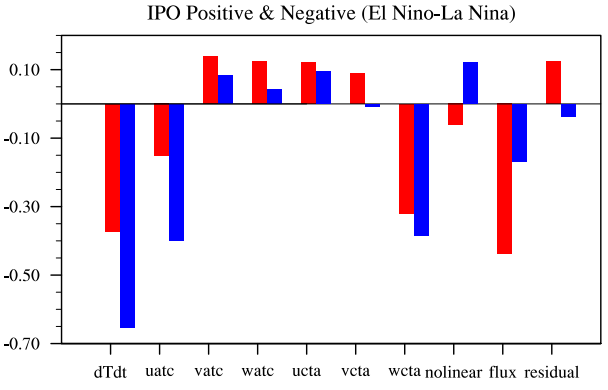

FIG. 10. The mixed layer heat budget terms of the El Niño minus La Niña composites for the positive (red bar; °C month^{-1}) and negative IPO (blue bar; °C month^{-1}) phases during ENSO decaying years from February(1) to June(1), averaged over the equatorial Pacific (3°S–3°N, 160°E–110°W). Each term in the figure represents the mixed layer temperature tendency ($dTdt$), advections of mean temperature by anomalous currents (uatc, vatc, and watc), advections of anomalous temperature by mean currents (ucta, vcta, and wcta), nonlinear temperature advection (nonlinear), heat flux (flux), and the residual, respectively.

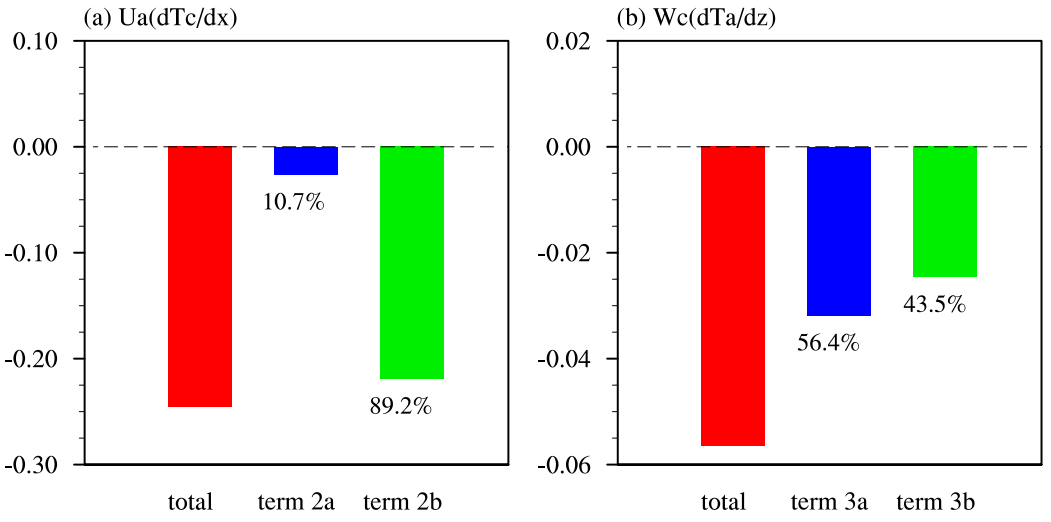

FIG. 11. The El Niño minus La Niña composites (°C month^{-1}) for (a) three terms in Eq. (2) and (b) three terms in Eq. (3). The relative contribution of the individual term is marked with percentages.

tendency (Jin and An 1999), responsible for the growth and phase transitions of ENSO. This clearly shows that the faster ENSO decay in the negative IPO phase in comparison with the positive phase, is mainly contributed by both stronger zonal advective and thermocline feedback processes (Fig. 10). The term of the net surface heat flux makes a negative contribution to the different ENSO decaying speeds between the two IPO phases. Other terms play minor roles with regard to the tendency of the mixed layer sea temperature associated with ENSO. To avoid possible impacts from the ENSO amplitude, the normalized heat budget is examined and the results remain almost the same (not shown). The zonal advective and thermocline feedbacks are emphasized to discuss their difference in the next analyses.

To understand the major source of differences between the positive and negative IPO phases for these two feedbacks, the direct (mean state changes represented by W_c and $\partial T_c/\partial x$) and indirect (ENSO variability changes dependent on the mean state represented by U_a and $\partial T_a/\partial z$) contributions of the IPO are evaluated. For zonal advective feedbacks, their differences between the two IPO phases can be formulated as

$$\underbrace{U_{a_2}\frac{\partial T_{c_2}}{\partial x}-U_{a_1}\frac{\partial T_{c_1}}{\partial x}}_{\text{total difference}}=\underbrace{U_{a_0}\left(\frac{\partial T_{c_2}}{\partial x}-\frac{\partial T_{c_1}}{\partial x}\right)}_{\text{term 2a}}+\underbrace{\frac{\partial T_{c_0}}{\partial x}(U_{a_2}-U_{a_1})}_{\text{term 2b}}, \tag{2}$$

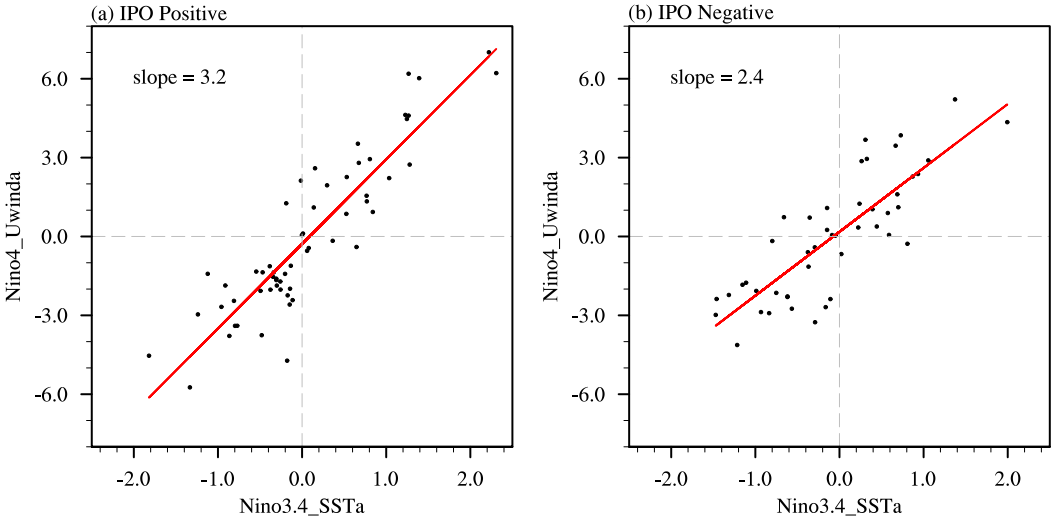

FIG. 12. Scatterplot between the zonal wind anomalies (m s^{-1}) of the Niño-4 region (5°S–5°N, 160°E–150°W) and the Niño-3.4 index (°C) during ENSO mature seasons (DJF) in the (a) positive and (b) negative IPO phases.

TABLE 2. The CMIP5 models used and four criteria for choosing models. Asterisks indicate that values or models meet the criteria. STD = standard deviation.

Number	Model name	ENSO STD	IPO STD	Correlation (ENSO and IOBW)	Maximum minus minimum
1	BCC-CSM1.1	0.82*	0.38*	0.29	0.81*
2	BNU-ESM	1.47	0.79*	0.64*	0.52*
3	CanESM2*	0.83*	0.50*	0.42*	0.84*
4	CMCC-CM*	0.64*	0.41*	0.44*	1.04*
5	CNRM-CM5*	0.85*	0.41*	0.61*	0.51*
6	ACCESS1.0*	0.66*	0.41*	0.51*	0.63*
7	CSIRO-Mk3.6.0	0.64*	0.50*	0.29	0.89*
8	FIO-ESM	1.22	0.67*	0.77*	0.47
9	EC-EARTH	0.47	0.36*	0.30	0.60*
10	INM-CM4.0	0.55	0.32	0.52*	0.53*
11	IPSL-CM5A-LR*	0.70*	0.53*	0.44*	0.83*
12	MIROC5*	0.87*	0.70*	0.49*	0.78*
13	HadGEM2-ES*	0.71*	0.57*	0.42*	0.99*
14	MPI-ESM-P*	0.80*	0.60*	0.59*	0.67*
15	MRI-CGCM3	0.58	0.36*	0.38	1.08*
16	GISS-E2-R-CC	0.55	0.33	0.38	0.90*
17	CCSM4	1.04	0.71*	0.37	0.77*
18	CESM1-CAM5*	0.96*	0.65*	0.41*	0.82*
19	NorESM1-ME	0.90*	0.63*	0.69*	0.31
20	GFDL-ESM2M	1.21	0.83*	0.72*	0.28

where the subscripts 1, 2, and 0 denote values in the positive and negative phases and their average, respectively. The left-hand side term indicates the total differences of $U_a(\partial T_c/\partial x)$ between the two phases. The other two terms, which are labeled as "term 2a" and "term 2b", are associated with the differences induced by mean state changes (term 2a) and ENSO variability changes (term 2b), respectively. A similar decomposition for thermocline feedbacks can also be expressed as

$$\underbrace{W_{c_2}\frac{\partial T_{a_2}}{\partial z}-W_{c_1}\frac{\partial T_{a_1}}{\partial z}}_{\text{total difference}}=\underbrace{\frac{\partial T_{a_0}}{\partial z}(W_{c_2}-W_{c_1})}_{\text{term 3a}}+\underbrace{W_{c_0}\left(\frac{\partial T_{a_2}}{\partial z}-\frac{\partial T_{a_1}}{\partial z}\right)}_{\text{term 3b}}. \quad (3)$$

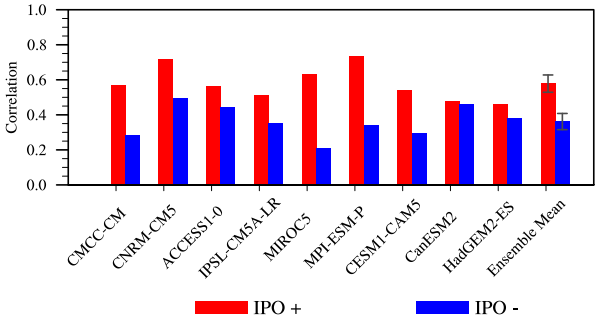

FIG. 13. Correlations between the Niño-3.4 index and TIOI in the positive (red bar) and negative (blue bar) IPO phases for nine CMIP5 models and their ensemble mean. The error bars represent one standard deviation.

Each term of $U_a(\partial T_c/\partial x)$ and $W_c(\partial T_a/\partial z)$ is calculated and shown in Figs. 11a and 11b, respectively. Note that the El Niño minus La Niña composites are applied for all the terms and the relative contribution from the individual one is also displayed. As shown in Fig. 11a, the difference of $U_a(\partial T_c/\partial x)$ is mainly contributed by ENSO variability changes (term 2b), while 10.7% of the contribution is from the mean state changes (term 2a). Different from the zonal advective feedback, both terms associated with $W_c(\partial T_a/\partial z)$ display comparable contributions to the difference between the two IPO phases (Fig. 11b). According to previous studies, ENSO properties are highly dependent upon the background climate state (Fedorov and Philander 2000, 2001). Decadal changes of background state definitely can give rise to ENSO property changes despite the fact that the associated mechanism remains open (e.g., An and Jin 2000; Fedorov and Philander 2000; Wang and An 2002; Xiang et al. 2013; Kang et al. 2014; Hu and Fedorov 2018; Lin et al. 2018). As an example, Fig. 12 displays the different air–sea interactions in the positive and negative IPO phases, roughly measured as the relationship between the zonal wind anomalies over the equatorial central Pacific and the Niño-3.4 SSTA. A higher slope is observed during the ENSO mature season in the positive IPO phase than that in the negative phase, indicating a stronger ocean–atmosphere coupling. It suggests that various basic states could lead to different atmospheric–oceanic interactions in the Pacific, which could also contribute to different ENSO evolutions.

c. *ENSO–IOBW relationship in CMIP5 pi-Control simulations*

We further examine the IPO modulation of the ENSO–IOBW relationship in the pi-Control simulations from nine CMIP5 models. These nine models (marked with asterisks in Table 2) are

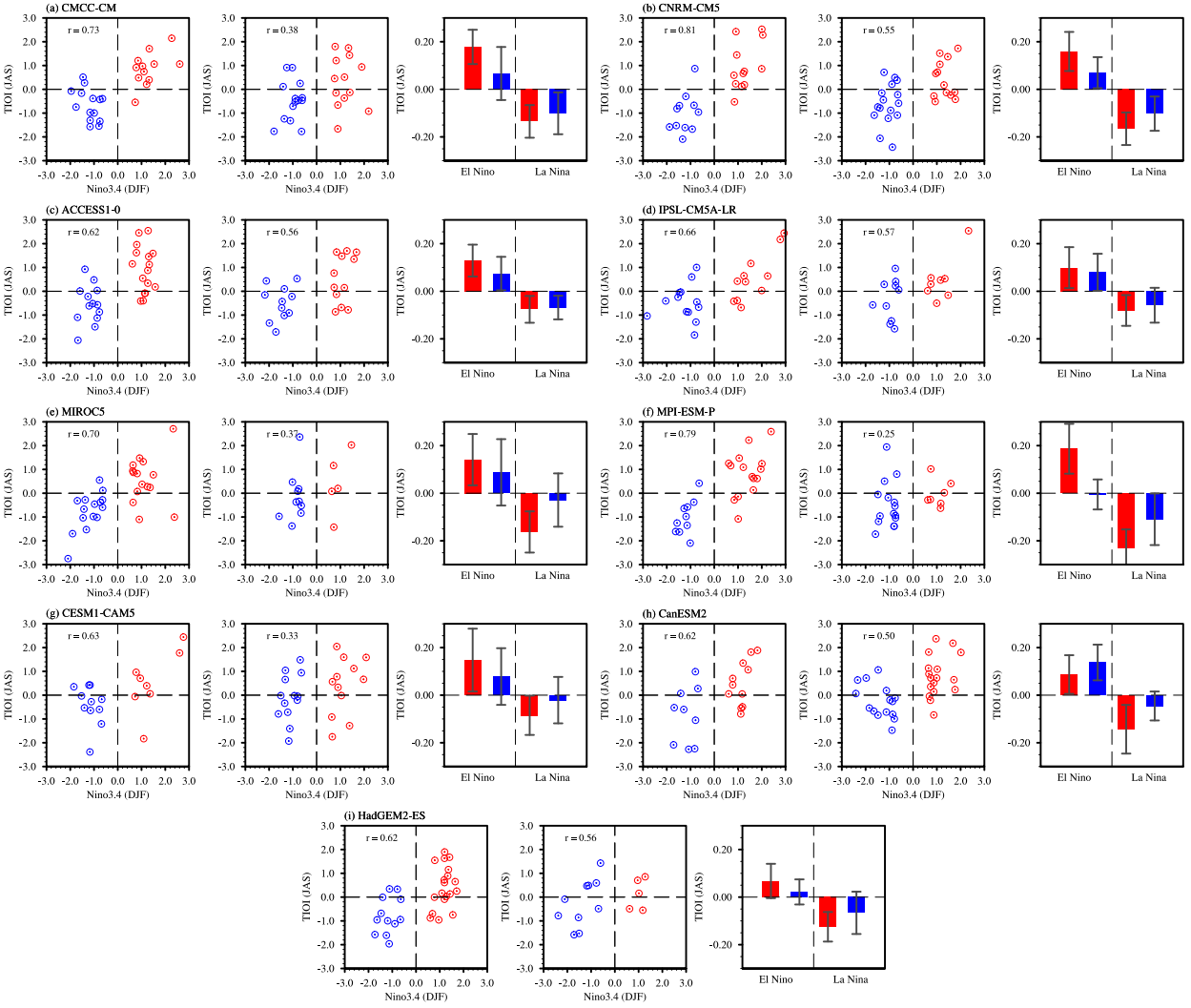

FIG. 14. As in Fig. 4, but for nine CMIP5 models.

selected from 20 CMIP5 models based on the following criteria. First, the simulated interannual variability of ENSO is limited to 0.8–1.2 times of that in observations, considering the crucial forcing effect of ENSO on the IO. Second, the simulated IPO variability is above 0.6 times of the observation, avoiding that too weak IPO variability in the models has a negligible modulation. Third, the correlation coefficient between the ENSO and IOBW should be above 0.4 (the critical value at 90% confidence level) since some models exaggerate or underestimate the ENSO impacts on the IO SSTA. Fourth, we consider the models with obvious decadal variations of the ENSO–IOBW relationship, which is roughly measured as the difference between maximum and minimum of sliding correlation coefficient being above 0.5. Figure 13 shows the ENSO–IOBW correlations in different IPO phases for nine models and their ensemble mean. Almost all models can capture a stronger ENSO–IOBW relationship during the positive IPO phase compared to the negative one, except that CanESM2 has less capability in simulating this characteristic. The difference in the ENSO–IOBW relationship is also confirmed by their ensemble mean (Fig. 13) and the scatterplot of the DJF Niño-3.4 and JAS TIOI during different IPO phases for each individual model (Fig. 14). Similar to the observation, most El Niño and La Niña events in the positive IPO phase are accompanied with warm and cold IO SSTA during their decaying summer, respectively. Their linear correlations exceed 95% confidence level in all the models. However, this linear relationship weakens a lot during the negative IPO phase. The nonstationary ENSO–IOBW relationship is also displayed in the composite cases. These model results support our hypothesis that the nonstationary ENSO–IOBW relationship is mainly modulated by the IPO. Furthermore, the Niño-3.4 SSTA difference in two IPO phases is also examined in the models for the ENSO decaying stage spanning from Apr(1) to Jun(1). A few models display stronger SSTA in the positive IPO phase than that in the negative phase, which is

partially related to different simulated ENSO amplitudes (not shown).

5. Conclusions and discussion

In the present study, the interdecadal modulation of the ENSO–IOBW relationship by the IPO and its possible mechanisms are investigated based on the observations and CMIP5 simulations. Striking SSTA differences are detected over the equatorial IO in the summer (JAS) following the decay phase of ENSO between the positive and negative IPO phases. The 17-yr sliding correlation between winter ENSO and the subsequent summer IOBW varies consistently with the IPO phase, displaying a significant positive correlation ($R = 0.79$) during the positive IPO phase but an insignificant correlation during the negative phase. Most El Niño and La Niña winters during the positive IPO phase are accompanied by significant warm and cold SSTA over the equatorial IO in the late summer, respectively. In comparison, the teleconnections of either El Niño or La Niña events to the IO weaken a lot during the negative IPO phase.

The nonstationary ENSO–IOBW relationship seems to be attributed to the different decaying speeds of ENSO due to different IPO phases. ENSO events in the positive IPO phase decay more slowly compared to the ones in the negative phase and delay their transitions both from a warm to a cold state and a cold to a warm state. The slow decay of El Niño events thereby promotes a longer persistent warming over the equatorial IO through summer via the atmospheric bridge, and similar results are shown for La Niña events. Our heat budget analyses in the tropical Pacific suggest that the decay process of ENSO is largely controlled by the zonal advective and thermocline feedbacks. Both oceanic processes are stronger in the negative IPO phase than in the positive one, and their differences are mainly due to the mean state changes and the associated ENSO variability changes. This IPO modulation of the ENSO–IOBW relationship is well reproduced by nine CMIP5 models, which capture the observed features relatively well.

We have shown that the strong IPO modulation of the interbasin relationship exists between the tropical Pacific and Indian Oceans. The mean state changes associated with the IPO can directly influence the ENSO-associated oceanic processes and thus modify the ENSO decaying speed. Simultaneously, the mean state can also modulate the ENSO variability, which further has an important role in the ENSO evolution. However, how the mean climate state influences ENSO properties is not well understood and fundamental mechanisms deserve further investigation. In addition, the IO SSTA has remarkable climate impacts over surrounding regions during summer seasons. For example, the IO SSTA can excite anticyclonic anomalies over the WNP during the ENSO decaying summer (Yang et al. 2007; Xie et al. 2009, 2016), which further affects the East Asian climate. The summer IO SSTA also plays an important role in influencing the Indian–Australian summer monsoon on biennial time scales (Meehl 1997; Yoo et al. 2006). Our work demonstrates that the summer IO SSTA exhibits a nonstationary relationship with ENSO, which can be largely explained by the mean state changes due to the IPO. It carries important implications for the seasonal prediction of the IO SSTA and associated summer climate anomalies.

Acknowledgments. This work was supported by the second Tibetan Plateau Scientific Expedition and Research program (2019QZKK0105), and the National Key Research and Development Program (2018YFC1506002).

REFERENCES

Alexander, M. A., I. Bladé, M. Newman, J. R. Lanzante, N.-C. Lau, and J. D. Scott, 2002: The atmospheric bridge: The influence of ENSO teleconnections on air–sea interaction over the global oceans. *J. Climate*, **15**, 2205–2231, https://doi.org/10.1175/1520-0442(2002)015<2205:TABTIO>2.0.CO;2.

An, S.-I., and F.-F. Jin, 2000: An eigen analysis of the interdecadal changes in the structure and frequency of ENSO mode. *Geophys. Res. Lett.*, **27**, 2573–2576, https://doi.org/10.1029/1999GL011090.

——, and ——, 2004: Nonlinearity and asymmetry of ENSO. *J. Climate*, **17**, 2399–2412, https://doi.org/10.1175/1520-0442(2004)017<2399:NAAOE>2.0.CO;2.

Annamalai, H., R. Murtugudde, J. Potemra, S. P. Xie, P. Liu, and B. Wang, 2003: Coupled dynamics over the Indian Ocean: Spring initiation of the zonal mode. *Deep-Sea Res. II*, **50**, 2305–2330, https://doi.org/10.1016/S0967-0645(03)00058-4.

Bjerknes, J., 1969: Atmospheric teleconnections from the equatorial Pacific. *Mon. Wea. Rev.*, **97**, 163–172, https://doi.org/10.1175/1520-0493(1969)097<0163:ATFTEP>2.3.CO;2.

Cane, M. A., and S. E. Zebiak, 1985: A theory for El Niño and the Southern Oscillation. *Science*, **228**, 1085–1087, https://doi.org/10.1126/science.228.4703.1085.

Carton, J. A., G. A. Chepurin, and L. Chen, 2018: SODA3: A new ocean climate reanalysis. *J. Climate*, **31**, 6967–6983, https://doi.org/10.1175/JCLI-D-18-0149.1.

Chakravorty, S., J. S. Chowdary, and C. Gnanaseelan, 2012: Spring asymmetric mode in the tropical Indian Ocean: Role of El Niño and IOD. *Climate Dyn.*, **40**, 1467–1481, https://doi.org/10.1007/s00382-012-1340-1.

Chen, M., T. Li, X. Shen, and B. Wu, 2016: Relative roles of dynamic and thermodynamic processes in causing evolution asymmetry between El Niño and La Niña. *J. Climate*, **29**, 2201–2220, https://doi.org/10.1175/JCLI-D-15-0547.1.

Chen, W., B. Dong, and R. Lu, 2010: Impact of the Atlantic Ocean on the multidecadal fluctuation of El Niño–Southern Oscillation–South Asian monsoon relationship in a coupled general circulation model. *J. Geophys. Res.*, **115**, D17109, https://doi.org/10.1029/2009JD013596.

Chowdary, J. S., S.-P. Xie, H. Tokinaga, Y. M. Okumura, H. Kubota, N. Johnson, and X.-T. Zheng, 2012: Interdecadal variations in ENSO teleconnection to the Indo–western Pacific for 1870–2007. *J. Climate*, **25**, 1722–1744, https://doi.org/10.1175/JCLI-D-11-00070.1.

——, A. Parekh, C. Gnanaseelan, and P. Sreenivas, 2014: Interdecadal modulation of ENSO teleconnections to the Indian Ocean in a coupled model: Special emphasis on decay phase of El Niño. *Global Planet. Change*, **112**, 33–40, https://doi.org/10.1016/j.gloplacha.2013.11.003.

Compo, G. P., and Coauthors, 2011: The Twentieth Century Reanalysis Project. *Quart. J. Roy. Meteor. Soc.*, **137** (654), 1–28, https://doi.org/10.1002/qj.776.

Du, Y., S.-P. Xie, G. Huang, and K. Hu, 2009: Role of air–sea interaction in the long persistence of El Niño–induced north

Indian Ocean warming. *J. Climate*, **22**, 2023–2038, https://doi.org/10.1175/2008JCLI2590.1.

——, ——, Y.-L. Yang, X.-T. Zheng, L. Liu, and G. Huang, 2013: Indian Ocean variability in the CMIP5 multimodel ensemble: The basin mode. *J. Climate*, **26**, 7240–7266, https://doi.org/10.1175/JCLI-D-12-00678.1.

Duchon, C. E., 1979: Lanczos filtering in one and two dimensions. *J. Appl. Meteor.*, **18**, 1016–1022, https://doi.org/10.1175/1520-0450(1979)018<1016:LFIOAT>2.0.CO;2.

Enfield, D. B., A. M. Mestas-Nuñez, and P. J. Trimble, 2001: The Atlantic Multidecadal Oscillation and its relation to rainfall and river flows in the continental U.S. *Geophys. Res. Lett.*, **28**, 2077–2080, https://doi.org/10.1029/2000GL012745.

Fedorov, A. V., and S. G. Philander, 2000: Is El Niño changing? *Science*, **288**, 1997–2002, https://doi.org/10.1126/science.288.5473.1997.

——, and ——, 2001: A stability analysis of tropical ocean–atmosphere interactions: Bridging measurements and theory for El Niño. *J. Climate*, **14**, 3086–3101, https://doi.org/10.1175/1520-0442(2001)014<3086:ASAOTO>2.0.CO;2.

Feng, J., L. Wang, and W. Chen, 2014: How does the East Asian summer monsoon behave in the decaying phase of El Niño during different PDO phases? *J. Climate*, **27**, 2682–2698, https://doi.org/10.1175/JCLI-D-13-00015.1.

Geng, X., W. Zhang, M. F. Stuecker, P. Liu, F.-F. Jin, and G. Tan, 2017: Decadal modulation of the ENSO–East Asian winter monsoon relationship by the Atlantic Multidecadal Oscillation. *Climate Dyn.*, **49**, 2531–2544, https://doi.org/10.1007/s00382-016-3465-0.

——, ——, F.-F. Jin, and M. F. Stuecker, 2018: A new method for interpreting nonstationary running correlations and its application to the ENSO–EAWM relationship. *Geophys. Res. Lett.*, **45**, 327–334, https://doi.org/10.1002/2017GL076564.

Harrison, D. E., and N. K. Larkin, 1996: The COADS sea level pressure signal: A near-global El Niño composite and time series view, 1946–1993. *J. Climate*, **9**, 3025–3055, https://doi.org/10.1175/1520-0442(1996)009<3025:TCSLPS>2.0.CO;2.

Henley, B. J., J. Gergis, D. J. Karoly, S. Power, J. Kennedy, and C. K. Folland, 2015: A tripole index for the Interdecadal Pacific Oscillation. *Climate Dyn.*, **45**, 3077–3090, https://doi.org/10.1007/s00382-015-2525-1.

Hersbach, H., and Coauthors, 2020: The ERA5 global reanalysis. *Quart. J. Roy. Meteor. Soc.*, **146**, 1999–2049, https://doi.org/10.1002/qj.3803.

Hu, S., and A. V. Fedorov, 2018: Cross-equatorial winds control El Niño diversity and change. *Nat. Climate Change*, **8**, 798–802, https://doi.org/10.1038/s41558-018-0248-0.

Huang, G., K. Hu, and S.-P. Xie, 2010: Strengthening of tropical Indian Ocean teleconnection to the northwest Pacific since the mid-1970s: An atmospheric GCM study. *J. Climate*, **23**, 5294–5304, https://doi.org/10.1175/2010JCLI3577.1.

Jin, F.-F., 1997: An equatorial ocean recharge paradigm for ENSO. Part I: Conceptual model. *J. Atmos. Sci.*, **54**, 811–829, https://doi.org/10.1175/1520-0469(1997)054<0811:AEORPF>2.0.CO;2.

——, and S.-I. An, 1999: Thermocline and zonal advective feedbacks within the equatorial ocean recharge oscillator model for ENSO. *Geophys. Res. Lett.*, **26**, 2989–2992, https://doi.org/10.1029/1999GL002297.

Kang, I.-S., H. No, and F. Kucharski, 2014: ENSO amplitude modulation associated with the mean SST changes in the tropical central Pacific induced by Atlantic multidecadal oscillation. *J. Climate*, **27**, 7911–7920, https://doi.org/10.1175/JCLI-D-14-00018.1.

Klein, S. A., B. J. Soden, and N.-C. Lau, 1999: Remote sea surface temperature variations during ENSO: Evidence for a tropical atmospheric bridge. *J. Climate*, **12**, 917–932, https://doi.org/10.1175/1520-0442(1999)012<0917:RSSTVD>2.0.CO;2.

Knight, J. R., 2005: A signature of persistent natural thermohaline circulation cycles in observed climate. *Geophys. Res. Lett.*, **32**, L20708, https://doi.org/10.1029/2005GL024233.

Krishnamurthy, V., and B. P. Kirtman, 2003: Variability of the Indian Ocean: Relation to monsoon and ENSO. *Quart. J. Roy. Meteor. Soc.*, **129**, 1623–1646, https://doi.org/10.1256/qj.01.166.

Lau, N.-C., and M. J. Nath, 2003: Atmosphere–ocean variations in the Indo-Pacific sector during ENSO episodes. *J. Climate*, **16**, 3–20, https://doi.org/10.1175/1520-0442(2003)016<0003:AOVITI>2.0.CO;2.

Li, T., B. Wang, C. P. Chang, and Y. Zhang, 2003: A theory for the Indian Ocean dipole–zonal mode. *J. Atmos. Sci.*, **60**, 2119–2135, https://doi.org/10.1175/1520-0469(2003)060<2119:ATFTIO>2.0.CO;2.

Lin, R., F. Zheng, and X. Dong, 2018: ENSO frequency asymmetry and the Pacific decadal oscillation in observations and 19 CMIP5 models. *Adv. Atmos. Sci.*, **35**, 495–506, https://doi.org/10.1007/s00376-017-7133-z.

Liu, Z., and M. Alexander, 2007: Atmospheric bridge, oceanic tunnel, and global climatic teleconnections. *Rev. Geophys.*, **45**, RG2005, https://doi.org/10.1029/2005RG000172.

Lu, R., W. Chen, and B. Dong, 2008: How does a weakened Atlantic thermohaline circulation lead to an intensification of the ENSO–South Asian summer monsoon interaction? *Geophys. Res. Lett.*, **35**, L08706, https://doi.org/10.1029/2008GL033394.

Mantua, N. J., S. R. Hare, Y. Zhang, J. M. Wallace, and R. C. Francis, 1997: A Pacific interdecadal climate oscillation with impacts on salmon production. *Bull. Amer. Meteor. Soc.*, **78**, 1069–1079, https://doi.org/10.1175/1520-0477(1997)078<1069:APICOW>2.0.CO;2.

Meehl, G. A., 1997: The South Asian monsoon and the tropospheric biennial oscillation. *J. Climate*, **10**, 1921–1943, https://doi.org/10.1175/1520-0442(1997)010<1921:TSAMAT>2.0.CO;2.

Neelin, J. D., D. S. Battisti, A. C. Hirst, F.-F. Jin, Y. Wakata, T. Yamagata, and S. E. Zebiak, 1998: ENSO theory. *J. Geophys. Res.*, **103**, 14 261–14 290, https://doi.org/10.1029/97JC03424.

Nigam, S., and H.-S. Shen, 1993: Structure of oceanic and atmospheric low-frequency variability over the tropical Pacific and Indian Oceans. Part I: COADS observations. *J. Climate*, **6**, 657–676, https://doi.org/10.1175/1520-0442(1993)006<0657:SOOAAL>2.0.CO;2.

Power, S., T. Casey, C. Folland, A. Colman, and V. Mehta, 1999: Inter-decadal modulation of the impact of ENSO on Australia. *Climate Dyn.*, **15**, 319–324, https://doi.org/10.1007/s003820050284.

Rayner, N. A., D. E. Parker, E. B. Horton, C. K. Folland, L. V. Alexander, D. P. Rowell, E. C. Kent, and A. Kaplan, 2003: Global analyses of sea surface temperature, sea ice, and night marine air temperature since the late nineteenth century. *J. Geophys. Res.*, **108**, 4407, https://doi.org/10.1029/2002JD002670.

Saji, N. H., B. N. Goswami, P. N. Vinayachandran, and T. Yamagata, 1999: A dipole mode in the tropical Indian Ocean. *Nature*, **401**, 360–363, https://doi.org/10.1038/43854.

——, S. P. Xie, and T. Yamagata, 2006: Tropical Indian Ocean variability in the IPCC twentieth-century climate simulations. *J. Climate*, **19**, 4397–4417, https://doi.org/10.1175/JCLI3847.1.

Schott, F. A., S.-P. Xie, and J. P. McCreary, 2009: Indian Ocean circulation and climate variability. *Rev. Geophys.*, **47**, RG1002, https://doi.org/10.1029/2007RG000245.

Stuecker, M. F., F.-F. Jin, A. Timmermann, and S. McGregor, 2015: Combination mode dynamics of the anomalous northwest Pacific anticyclone. *J. Climate*, **28**, 1093–1111, https://doi.org/10.1175/JCLI-D-14-00225.1.

Tao, W., G. Huang, K. Hu, X. Qu, G. Wen, and H. Gong, 2015: Interdecadal modulation of ENSO teleconnections to the Indian Ocean Basin Mode and their relationship under global warming in CMIP5 models. *Int. J. Climatol.*, **35**, 391–407, https://doi.org/10.1002/joc.3987.

Trenberth, K. E., G. W. Branstator, D. Karoly, A. Kumar, N.-C. Lau, and C. Ropelewski, 1998: Progress during TOGA in understanding and modeling global teleconnections associated with tropical sea surface temperatures. *J. Geophys. Res.*, **103**, 14 291–14 324, https://doi.org/10.1029/97JC01444.

Wallace, J. M., and D. S. Gutzler, 1981: Teleconnections in the geopotential height field during the Northern Hemisphere winter. *Mon. Wea. Rev.*, **109**, 784–812, https://doi.org/10.1175/1520-0493(1981)109<0784:TITGHF>2.0.CO;2.

Wang, B., and S.-I. An, 2002: A mechanism for decadal changes of ENSO behavior: Roles of background wind changes. *Climate Dyn.*, **18**, 475–486, https://doi.org/10.1007/s00382-001-0189-5.

——, R. Wu, and X. Fu, 2000: Pacific–East Asian teleconnection: How does ENSO affect East Asian climate? *J. Climate*, **13**, 1517–1536, https://doi.org/10.1175/1520-0442(2000)013<1517:PEATHD>2.0.CO;2.

——, J. Yang, T. Zhou, and B. Wang, 2008: Interdecadal changes in the major modes of Asian–Australian monsoon variability: Strengthening relationship with ENSO since the late 1970s. *J. Climate*, **21**, 1771–1789, https://doi.org/10.1175/2007JCLI1981.1.

Wang, C., 2019: Three-ocean interactions and climate variability: A review and perspective. *Climate Dyn.*, **53**, 5119–5136, https://doi.org/10.1007/s00382-019-04930-x.

Watanabe, M., and F.-F. Jin, 2002: Role of Indian Ocean warming in the development of Philippine Sea anticyclone during ENSO. *Geophys. Res. Lett.*, **29**, 1478, https://doi.org/10.1029/2001GL014318.

Watanabe, T., and K. Yamazaki, 2014: Decadal-scale variation of South Asian summer monsoon onset and its relationship with the Pacific decadal oscillation. *J. Climate*, **27**, 5163–5173, https://doi.org/10.1175/JCLI-D-13-00541.1.

Weare, B. C., 1979: A statistical study of the relationships between ocean surface temperatures and the Indian monsoon. *J. Atmos. Sci.*, **36**, 2279–2291, https://doi.org/10.1175/1520-0469(1979)036<2279:ASSOTR>2.0.CO;2.

Webster, P. J., A. M. Moore, J. P. Loschnigg, and R. R. Leben, 1999: Coupled ocean–atmosphere dynamics in the Indian Ocean during 1997–98. *Nature*, **401**, 356–360, https://doi.org/10.1038/43848.

Wu, R., and S.-W. Yeh, 2010: A further study of the tropical Indian Ocean asymmetric mode in boreal spring. *J. Geophys. Res.*, **115**, D08101, https://doi.org/10.1029/2009JD012999.

——, B. P. Kirtman, and V. Krishnamurthy, 2008: An asymmetric mode of tropical Indian Ocean rainfall variability in boreal spring. *J. Geophys. Res.*, **113**, D05104, https://doi.org/10.1029/2007JD009316.

Wyrtki, K., 1975: El Niño—The dynamic response of the equatorial Pacific Ocean to atmospheric forcing. *J. Phys. Oceanogr.*, **5**, 572–584, https://doi.org/10.1175/1520-0485(1975)005<0572:ENTDRO>2.0.CO;2.

Xiang, B., B. Wang, and T. Li, 2013: A new paradigm for the predominance of standing central Pacific warming after the late 1990s. *Climate Dyn.*, **41**, 327–340, https://doi.org/10.1007/s00382-012-1427-8.

Xie, S.-P., H. Annamalai, F. A. Schott, and J. P. Mccreary, 2002: Structure and mechanisms of South Indian Ocean climate variability. *J. Climate*, **15**, 864–878, https://doi.org/10.1175/1520-0442(2002)015<0864:SAMOSI>2.0.CO;2.

——, K. Hu, J. Hafner, H. Tokinaga, Y. Du, G. Huang, and T. Sampe, 2009: Indian Ocean capacitor effect on Indo–western Pacific climate during the summer following El Niño. *J. Climate*, **22**, 730–747, https://doi.org/10.1175/2008JCLI2544.1.

——, Y. Du, G. Huang, X.-T. Zheng, H. Tokinaga, K. Hu, and Q. Liu, 2010: Decadal shift in El Niño influences on Indo–western Pacific and East Asian climate in the 1970s. *J. Climate*, **23**, 3352–3368, https://doi.org/10.1175/2010JCLI3429.1.

——, K. Yu, D. U. Yan, H. U. Kaiming, J. S. Chowdary, and G. Huang, 2016: Indo-western Pacific Ocean capacitor and coherent climate anomalies in post-ENSO summer: A review. *Adv. Atmos. Sci.*, **33**, 411–432, https://doi.org/10.1007/s00376-015-5192-6.

Yang, J., Q. Liu, S.-P. Xie, Z. Liu, and L. Wu, 2007: Impact of the Indian Ocean SST basin mode on the Asian summer monsoon. *Geophys. Res. Lett.*, **34**, L02708, https://doi.org/10.1029/2006GL028571.

Yang, Y., S.-P. Xie, Y. Du, and H. Tokinaga, 2015: Interdecadal difference of interannual variability characteristics of South China Sea SSTs associated with ENSO. *J. Climate*, **28**, 7145–7160, https://doi.org/10.1175/JCLI-D-15-0057.1.

Yoo, S.-H., S. Yang, and C.-H. Ho, 2006: Variability of the Indian Ocean sea surface temperature and its impacts on Asian-Australian monsoon climate. *J. Geophys. Res.*, **111**, D03108, https://doi.org/10.1029/2005JD006001.

Yu, J.-Y., and K. M. Lau, 2004: Contrasting Indian Ocean SST variability with and without ENSO influence: A coupled atmosphere–ocean GCM study. *Meteor. Atmos. Phys.*, **90**, 179–191, https://doi.org/10.1007/s00703-004-0094-7.

Zhang, R., A. Sumi, and M. Kimoto, 1996: Impact of El Niño on the East Asian monsoon. *J. Meteor. Soc. Japan*, **74**, 49–62, https://doi.org/10.2151/jmsj1965.74.1_49.

Zhang, W., F.-F. Jin, J.-X. Zhao, and J. Li, 2013: On the bias in simulated ENSO SSTA meridional widths of CMIP3 models. *J. Climate*, **26**, 3173–3186, https://doi.org/10.1175/JCLI-D-12-00347.1.

——, H. Li, M. F. Stuecker, F.-F. Jin, and A. G. Turner, 2016: A new understanding of El Niño's impact over East Asia: Dominance of the ENSO combination mode. *J. Climate*, **29**, 4347–4359, https://doi.org/10.1175/JCLI-D-15-0104.1.